

# DFT-Computational Modeling and TiberCAD Frameworks for Photovoltaic Performance Investigation of Copper-Based 2D Hybrid Perovskite Solar Absorbers

Bilel Chouchen, Nouredine Mhadhbi, Bouzid Gassoumi, Intissar Hamdi, Hamid Hadi, Matthias Auf der Maur, Abdelkader Chouaih, Taoufik Ladhari, Salvatore Magazù, Houcine Naili,\* and Sahbi Ayachi\*



Cite This: *ACS Omega* 2024, 9, 29263–29273



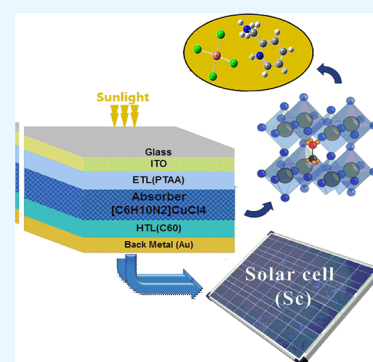
Read Online

ACCESS |

Metrics & More

Article Recommendations

**ABSTRACT:** In this work, we use a combination of dispersion-corrected density functional theory (DFT-D3) and the TiberCAD framework for the first time to investigate a newly designed and synthesized class of  $(C_6H_{10}N_2)[CuCl_4]$  2D-type perovskite. The inter- and intra-atomic reorganization in the crystal packing and the type of interaction forming in the active area have been discussed via Hirshfeld surface (HS) analyses. A distinct charge transfer from  $CuCl_4$  to  $[C_6H_{10}N_2]$  is identified by frontier molecular orbitals (FMOs) and density of states (DOS). This newly designed narrow-band gap small-molecule perovskite, with an energy gap ( $E_g$ ) of 2.11 eV, exhibits a higher fill factor (FF = 81.34%), leading to an open-circuit voltage ( $V_{oc}$ ) of 1.738 V and a power conversion efficiency (PCE) approaching ~10.20%. The interaction between a donor (D) and an acceptor (A) results in a charge transfer complex (CT) through the formation of hydrogen bonds (Cl–H), as revealed by QTAIM analysis. These findings were further supported by 2D-LOL and 3D-ELF analyses by visualizing excess electrons surrounding the acceptor entity. Finally, we performed numerical simulations of solar cell structures using TiberCAD software.



## 1. INTRODUCTION

Organic hybrid perovskites have received significant attention over the past decade due to their potential applications in optoelectronic and photovoltaic devices. Notably, they are full under the classifications of third generation cells, representing advancements in the manufacturing process, and are considered a more environmentally friendly alternative to silicon-based solar cell.<sup>1,2</sup> Despite the exceptional performance of organic–inorganic hybrid materials, two major drawbacks can prevent their commercial applications in electronic devices. First, stability remains a critical concern, particularly associated with the choice of organic cations. The hygroscopic nature of organic cations, such as (methylamine ( $MA^+$ ) and formamidine ( $FA^+$ ), poses challenges when exposed to oxygen in high-temperature and high-humidity conditions.<sup>3,4</sup> Second, lead-based halides are highly toxic and pose significant risk to human health and the environment.<sup>5,6</sup> To address this issue, various approaches have been developed including substituting the organic cation with an inorganic one to improve their stability.<sup>7,8</sup> Additionally, numerous numerical and experimentally based studies on alternative perovskites, such as  $CsPbI_2Br$ ,  $Cs_2AgBiI_6$ , and  $CH_3NH_3PbX_3$ , have demonstrated favorable electrical characteristics in the absorber region of the cell system.<sup>9,10</sup> In single junction cells based on perovskite material

(PSC), the power conversion efficiency (% PCE) has seen a notable improvement, ranging from 3.8% to 25.5%.<sup>11,12</sup> Various numerical studies on perovskite hybrid cells have been implemented using SCAPS 1-D software. For instance, Jayan et al.<sup>13</sup> reported maximum efficiency of 15% for  $CuSbS_2$  solar devices. Another robust simulation study, conducted using SCAPS-1D software demonstrated a PCE of 21.31% for  $CsPbI_3$  when utilized as an intrinsic layer.<sup>14,15</sup> The analysis of perovskite cell characteristics has specifically focused on the impact of the  $CH_3NH_3PbI_3$  absorber's thickness.

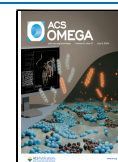
The optimal intrinsic thickness is identified as 0.9  $\mu m$ , falling within the range of 0.05 to 2  $\mu m$ . At this thickness, the characteristic parameters include a fill factor (FF) of 71.30%, a short-circuit current density ( $J_{sc}$ ) of 34  $mA/cm^2$ , and an open-circuit voltage ( $V_{oc}$ ) of 0.99 V.<sup>16</sup> Consequently, the overall efficiency for lead-free tin halide  $CH_3NH_3SnI_3$  is calculated to be 24.54%. In a related study, Hossain et al.<sup>17</sup> employed a

Received: January 6, 2024

Revised: April 7, 2024

Accepted: May 30, 2024

Published: June 25, 2024



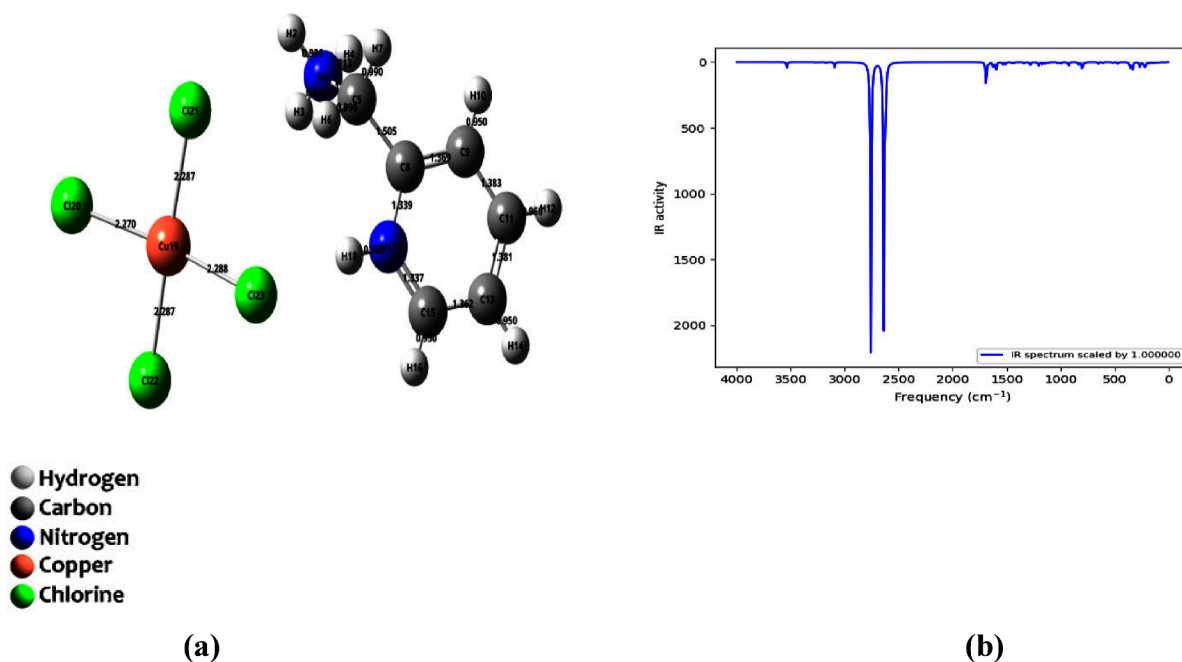


**Figure 1.** (a) Optimized structure and (b) FT-IR spectrum of the studied complex.

combination of DFT, SCAPS-1D, and wxAMPS to investigate the structural, optical, and electronic properties for optimizing the performance of a  $\text{Cs}_2\text{BiAgI}_6$ -based perovskite solar cell. Various materials were considered and compared for the electron transport layer (ETL) region, including PCBM, ZnO, and  $\text{TiO}_2$ , while  $\text{Cu}_2\text{O}$  and CuSc were evaluated for the hole transport layer (HTL) region. Results indicated that the maximum efficiency of 21.59% was achieved for ZnO as the best ETL, and CBTS as the best HTL. Further optimization possibilities in the performance of perovskite cells involve studying properties such as defect density, carrier recombination, and doping.<sup>18,19</sup> To achieve good stability and high reproducibility, minimizing defects in the perovskite layers is crucial. Yin et al.<sup>20</sup> have identified a theoretical effectiveness limit, including a defect concentration of less than  $3.64 \times 10^{15} \text{ cm}^{-3}$ . Despite the degradation of the perovskite (PVK) cell performance, some approaches have been proposed, such as the addition of an ITO layer. This not only enhances both the PCE and device stability, but also preserve optimal performance in challenging environmental conditions, including corrosion, humidity, and high temperature.<sup>21–23</sup> To understand the crystal-stability and the forces governing atomic organization in the studied compound, we present an analysis of inter- and intra-atomic interactions in our crystal packing through Hirshfeld surface (HS) analysis and density functional theory (DFT-D3).

The optoelectronic parameters crucial for studying solar cell applications are elucidated, focusing on the localization of HOMO/LUMO orbitals, gap energy ( $E_g$ ), and density of states (DOS). QTAIM analyses reveal the stabilization of the complex through two robust and two vdW-type interactions. The presence of Cl in proximity to  $\text{C}_6\text{H}_{10}\text{N}_2$  ensures the existence of delocalized electrons, facilitating the formation of a donor–acceptor system, thereby contributing to the complex's stability. The 3D-Electron Localization Function (3D-ELF) and the 2D-Localized Orbital Locator (2D-LOL) are tools used to explore the charge transfer between the two investigated systems.

Electrical parameters are focused on the study of the solar cell:  $\text{ITO}/\text{TiO}_2/(\text{C}_6\text{H}_{10}\text{N}_2)[\text{CuCl}_4]/\text{Spiro-OMeTAD}/\text{Au}$ . The impact of thickness and density of defects in the absorbing region has been investigated, revealing that the PCE of the PSCs can reach around 25%. Additionally, the increase in midgap is associated with a high defect density of  $10^{15} \text{ cm}^{-3}$ . In conclusion,  $(\text{C}_6\text{H}_{10}\text{N}_2)[\text{CuCl}_4]$  emerges as a promising material for new generation solar cells.

## 2. COMPUTATIONAL DETAILS

Theoretical calculations were conducted on copper perovskite  $(\text{C}_6\text{H}_{10}\text{N}_2)[\text{CuCl}_4]$  using Gaussian 09, rev. A.02.<sup>25</sup> Input files for Gaussian 09 were generated with GaussView 5.0.8<sup>26</sup> Becke's three-parameter Lee–Yang–Parr hybrid functional (B3LYP) was employed for all calculations. Dispersion-corrected density functional theory (DFT-D3)<sup>27,28</sup> at the level of theory (B3LYP/LANL2DZ)<sup>29–31</sup> was utilized for both geometry optimization and vibrational frequencies calculation of studied compound. The Hirshfeld surface (HS) mapping surfaces are the best method for considering the strong or weak interactions coexisting in a crystal, contributing to the system's stabilization. HS and 2D-fingerprint plots were calculated using Crystal Explorer 17.<sup>32</sup> This theory is involved in our discussion. Subsequently, the energy levels of frontier molecular orbitals (FMOs) ( $\epsilon_{\text{HOMO}}$  and  $\epsilon_{\text{LUMO}}$ ), energy gap ( $\Delta_{\text{H-L}}$ ), and density of states (DOS) were computed using the GaussSum03 program.<sup>33</sup> Optoelectronic properties, such as  $\lambda_{\text{max}}$  excitation energy ( $E_x$ ), and light-harvesting efficiency (LHE), were calculated by TD-DFT at the same level of theory. Furthermore, to assess the feasibility of experimentally forming the desired complex, the cohesive energy was calculated. Cohesive energy represents the amount of energy required to separate the components of a solid into neutral, free atoms. To deeply explore the types, nature, and strength of the forces that stabilize the studied system (as observed in the crystal packing HS), a topological QTAIM analysis was conducted. AIM parameters are generated using the Mutiwfn package.<sup>34</sup> The intra- and intersurface charge transfers of the

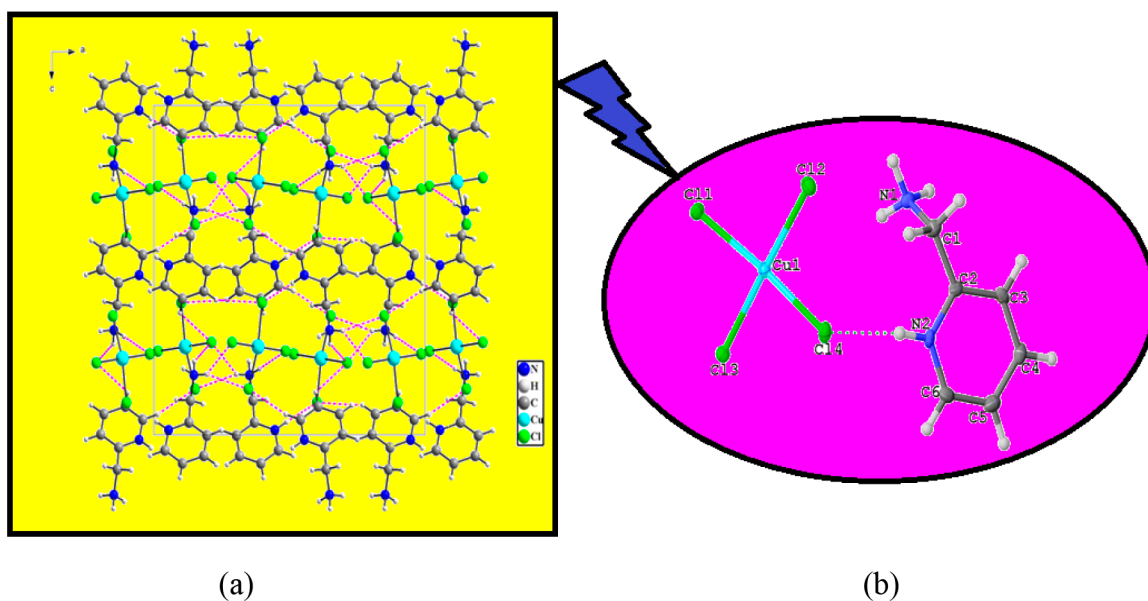


**Figure 2.** (a) Crystalline structure of  $(\text{C}_6\text{H}_{10}\text{N}_2)[\text{CuCl}_4]$  and (b) the unit cell of the 2D copper perovskite.

studied systems is thoroughly examined through ELF and LOL analyses. NCI-RDG theories are employed, applying color codes to identify the nature of interactions formed between  $\text{CuCl}_4$  and  $(\text{C}_6\text{H}_{10}\text{N}_2)$  materials.

Multiscale/multiphysics simulations are highly sought after in the analysis of electronic and optoelectronics devices such as III–V LEDs, organic diodes, transistors, and nanowire FETs.<sup>35,36</sup> TiberCad is one of the pioneering tools capable of addressing this need, spanning FEM continuous models to atomistic descriptions. The numerical modeling of the solar cell was conducted using TiberCAD Software<sup>37</sup> and is based on the semiclassical drift-diffusion transport model, which consists of the continuity equations of electrons (2)<sup>38</sup> and holes (3)<sup>39</sup> coupled via the Poisson eq 4 as follows:<sup>12</sup>

$$\frac{dP_n}{dt} = G_p - \frac{P_n - P_{n0}}{\tau_p} - p_n u_p \frac{dE}{dx} - u_p E \frac{dP_n}{dx} + D_n \frac{d^2 P_n}{dx^2} \quad (1)$$

$$\frac{dn_p}{dt} = G_n - \frac{n_p - n_{p0}}{\tau_p} - n_p u_n \frac{dE}{dx} - u_n E \frac{dn_p}{dx} + D_n \frac{d^2 n_p}{dx^2} \quad (2)$$

$$\frac{d}{dx} \left( \epsilon(x) \frac{d\phi}{dx} \right) = q [p(x) - n(x) + N_{d+}(x) - N_{a-}(x) + p_t(x) - n_t(x)] \quad (3)$$

where  $x$  represents the spatial coordinate along the material stack,  $q$  represents the electronic charge,  $G$  represents the generation rate,  $D$  represents the diffusion coefficient,  $\epsilon$  represents the dielectric permittivity,  $E$  represents the electric field,  $\phi$  represents the electrostatic potential,  $n(x)$  represents the number of free electrons,  $p(x)$  represents the number of holes,  $n_t(x)$  represents the number of trapped electrons,  $p_t(x)$  represents the number of trapped holes,  $N_{d+}$  represents the ionized donor doping concentration, and  $N_{a-}$  represents the acceptor ionized doping concentration.

### 3. RESULTS AND DISCUSSION

**3.1. Morphological Properties, Material Design, Electronic Behavior, And Binding Interaction Mechanism of the  $(\text{C}_6\text{H}_{10}\text{N}_2)[\text{CuCl}_4]$  Complex.** **3.1.1. Geometry Optimization, FT-IR, and HS Analyses.** The desired complex structure was optimized to attain stability, as illustrated in Figure 1. Imaginary frequencies and cohesive energy were examined, the primary factors influencing complex formation. The computed value of the cohesive energy ( $E_{\text{Coh}}$ ) was around  $98.72 \text{ kcal}\cdot\text{mol}^{-1}$ . The IR spectrum of the studied complex reveals positive vibrational frequencies with no observed imaginary frequency (refer to Figure 1). The obtained results, highlighting the high cohesive energy and the absence of the imaginary frequency, affirm the stability of the complex.

**3.1.2. Crystal Structure and Hirshfeld Surface (HS) Analyses.** 3D-Hirshfeld surface (HS) and 2D-fingerprint plot analyses have proven to be effective tools in determining the nature of intra- and intermolecular interaction in the crystalline form of the studied compound, utilizing well-defined color codes.<sup>40–44</sup> These analyses not only provide insights into the nature of interactions, but also efficiently represent the interaction sites where charge transfer between the two systems occurs.<sup>45–47</sup>

The distances between the HS and outside/inside atoms on the surface are denoted as  $d_e$  and  $d_i$ , respectively. The normalized distance  $d_{\text{norm}}$  is determined by the following equation:<sup>48,49</sup>

$$d_{\text{norm}} = \frac{d_i - r_i^{\text{vdw}}}{r_i^{\text{vdw}}} + \frac{d_e - r_e^{\text{vdw}}}{r_e^{\text{vdw}}} \quad (4)$$

The  $d_{\text{norm}}$  is symmetrically related to  $d_e$  and  $d_i$ , or the  $r_i^{\text{vdw}}$  and  $r_e^{\text{vdw}}$  characterized the vdW radii of the atom. In the HS surface mapping,  $d_{\text{norm}}$  reveals acceptor sites (negative region = nucleophilic sites) colored in red, while the positive region indicates donor sites (electrophilic regions), depicted in blue. Figure 2 illustrates the crystalline structure of the studied complex including our repetitive unit cell in this network. The 3D-HS figures of  $d_{\text{norm}}$ , shape index, and curvedness are presented in Figure 3a. Notably,  $d_{\text{norm}}$  ranges between  $-0.4472$



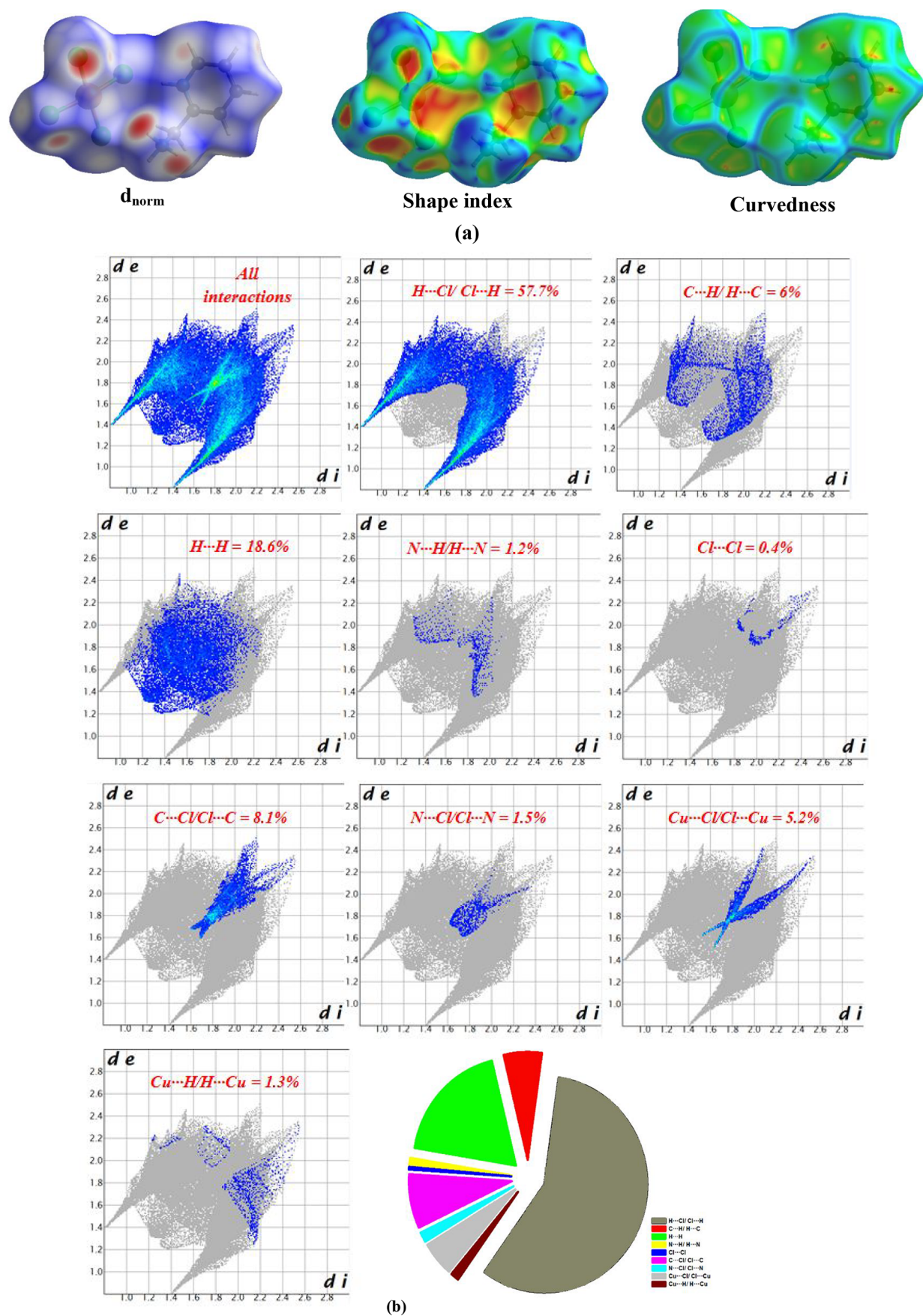
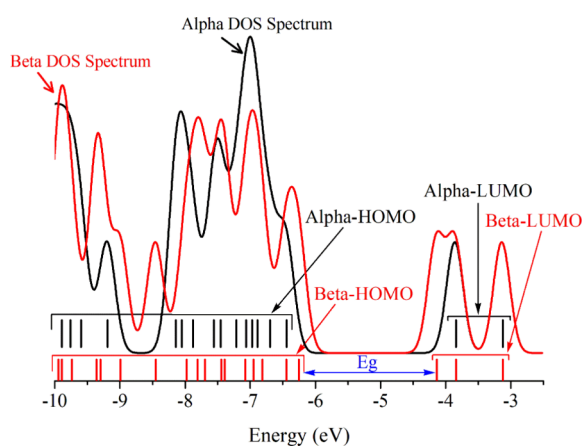


Figure 3. (a)  $d_{\text{norm}}$ , shape index, and curvedness and (b) the 2D-fingerprint plot analyses of the  $(\text{C}_6\text{H}_{10}\text{N}_2)[\text{CuCl}_4]$  complex.





**Figure 4.** Density of states (DOS) plot for the  $(\text{C}_6\text{H}_{10}\text{N}_2)[\text{CuCl}_4]$  complex.

and  $-0.8911 \text{ \AA}$ , the shape index is  $-1$  to  $1 \text{ \AA}$ , and the curvedness spans from  $-4$  to  $0.4 \text{ \AA}$ . Figure 3 also includes 2D-fingerprint plots illustrating the different main contacts of our complex in percentage. The analysis reveals that the most significant contribution to the overall crystal packing is attributed to the  $(\text{C}_6\text{H}_{10}\text{N}_2)[\text{CuCl}_4]$  complex, specifically,  $\text{H}\cdots\text{Cl}/\text{Cl}\cdots\text{H}$  interactions, constituting 57.7%. This site is highlighted in red in the  $d_{\text{norm}}$  and shape indexes, indicating it as an active site where an accumulation of electrons may foster H-binding interactions between the two systems. Figure 3b demonstrated that the  $\text{H}\cdots\text{H}$  interactions represent the second-largest contribution, comprising 18.6% of the total Hirshfeld surface. The interatomic contacts involving  $\text{C}\cdots\text{Cl}/\text{Cl}\cdots\text{C}/\text{Cu}\cdots\text{Cl}/\text{Cl}\cdots\text{Cu}$  and  $\text{C}\cdots\text{H}/\text{H}\cdots\text{C}$  exhibit lower contributions to crystal packing with percentages of 8.1% and 5.2%, respectively. This observation suggests that these interactions could be strengthened by the delocalization of electrons on the surfaces of the two systems, thereby stabilizing them. Contacts with the least contribution to crystal packing include  $\text{N}\cdots\text{Cl}/\text{Cl}\cdots\text{N}$ ,  $\text{Cu}\cdots\text{H}/\text{H}\cdots\text{Cu}$ ,  $\text{N}\cdots\text{H}/\text{H}\cdots\text{N}$ , and  $\text{Cl}\cdots\text{Cl}$ , with percentage contributions of 1.5%, 5.2%, 1.3%, 1.2%, and 0.4%, respectively. An important point emerging from the HS discussion is that the interaction promoting the stability of the complex is  $\text{Cl}\cdots\text{H}$ , indicating that the compound follows an electron donor–acceptor type interaction. This finding opens up an opportunity to explore the electronic properties of this material, proving to be valuable for novel photovoltaic cell applications.

**3.1.3. Electronic Parameters.** The HOMO and the LUMO, commonly referred to as frontier molecular orbitals (FMOs), play a crucial role in chemical reactions.<sup>50–52</sup> The energy gap ( $E_g = \Delta_{\text{H-L}}$ ) between these orbitals is a key indicator of the

chemical stability of the molecule.<sup>53</sup> Furthermore, it is essential for determining the optoelectronic properties of the molecule and its electrical transport characteristics (see Figure 4). The energy levels of the HOMO, LUMO, and  $E_g$  are given in Table 1. Additionally, a density of states (DOS) diagram for the complex under study was generated through GaussSum03 software, complementing the results of the FMOs analysis. The DOS reflects the number of different states in a unit energy range that can be occupied by electrons, providing valuable information about the electron distribution in FMOs.

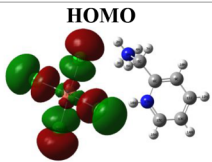
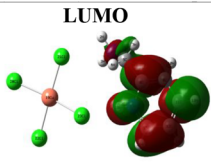
It is observed that localization of the HOMO orbitals completely surrounds the  $\text{CuCl}_4$  group. Subsequently, these electrons became delocalized around the second group ( $\text{C}_6\text{H}_{10}\text{N}_2$ ). Therefore, based on the HOMO–LUMO orbital localizations, our system is characterized as a donor (D)–acceptor (A) type. The electronic charge transfer (ECT), occurring between two systems, is a fundamental process and can enhance the stability of chemical entities through electrostatic interactions. This is subsequently confirmed by means of QTAIM analyses.

From Figure 4, it is evident that the DOS map features a bandgap of approximately 2.12 eV, separating the HOMO ( $\sim -6.25 \text{ eV}$ ) from the LUMO ( $\sim -4.13 \text{ eV}$ ).

**3.1.4. Optical Properties.** The optical characteristics and UV–visible spectrum of the  $(\text{C}_6\text{H}_{10}\text{N}_2)[\text{CuCl}_4]$  compound were computed by using the TD-DFT/B3LYP-D3/LanL2DZ level of theory, and results were visualized through the GaussSum03 program. The findings are illustrated in Figure 5 and Table 2, revealing three absorption peaks located at 499, 730, and 1021 nm, respectively. The high UV–visibility band (730 nm) is associated with the  $\pi \rightarrow \pi^*$  electronic transition, characterized by an optical energy gap of around 1.32 eV. Particularly, the optical spectrum shows a significant absorption band in the infrared range around  $1021 \text{ cm}^{-1}$ , probably due to intramolecular charge transfer. Moreover, the broad absorption range covering the entire visible region extending toward the infrared suggests the compound's potential for solar cell applications. According to Table 2, the major contribution of electronic transitions is from  $\text{H-2(A)} \rightarrow \text{LUMO(A)}$  (50%) and  $\text{H-1(B)} \rightarrow \text{LUMO(B)}$  (21%) with 50% and 21%, respectively. This result proves the possibility of crossing a set number of electrons at the same time from the HOMO to the LUMO bands, signifying a high energy/charge transfer on the material's surface and demonstrating the excellent absorbance capacity ( $1000 \text{ L}\cdot\text{mol}^{-1}\cdot\text{cm}^{-1}$ ) of the studied compound. This finding suggests that the  $(\text{C}_6\text{H}_{10}\text{N}_2)[\text{CuCl}_4]$  may serve as a new model for the next generation of photovoltaic applications.

The optical absorbance spectra of the  $(\text{C}_6\text{H}_{10}\text{N}_2)[\text{CuCl}_4]$  complex were experimentally obtained for both the film sample

**Table 1.** Energy Values of the Frontier Orbitals of HOMO–LUMO and the Energy Gap ( $E_g$ ) of the  $(\text{C}_6\text{H}_{10}\text{N}_2)[\text{CuCl}_4]$  Complex

HOMO	LUMO	Energy gap ( $E_g$ )
		
$-6.25 \text{ eV}$	$-4.13 \text{ eV}$	$2.12 \text{ eV}$

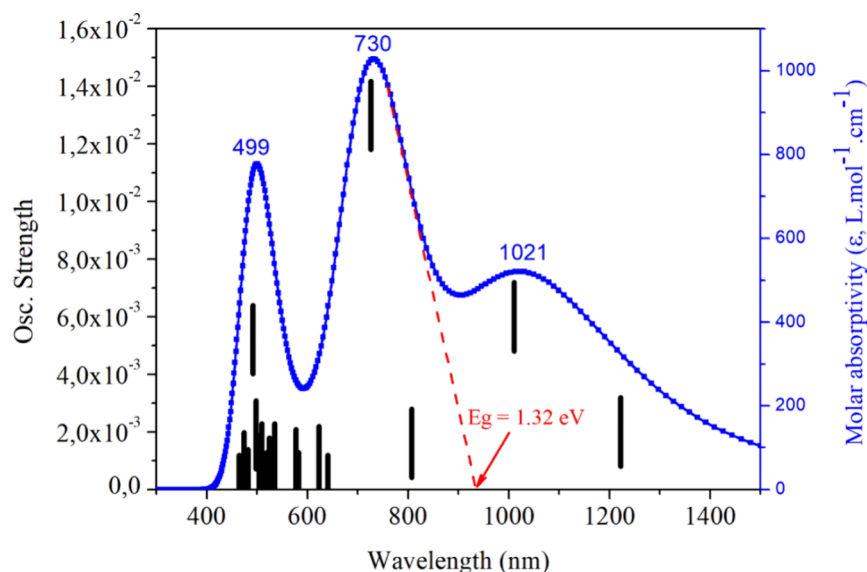


Figure 5. UV-visible absorption spectrum of the  $(C_6H_{10}N_2)[CuCl_4]$  complex.

**Table 2. Vertical Wavelength ( $\lambda$ , nm) and the Oscillator Strengths ( $f$ ) Contributing to  $S_0 \rightarrow S_1$  Electronic Transitions for the Investigated  $(C_6H_{10}N_2)[CuCl_4]$  Complex, Computed by the TD-B3LYP/LANL2DZ Method<sup>a</sup>**

$\lambda_{max}^{abs}$ (nm)	$f_{max}$	major contribs (%)	minor contribs (%)
499	0.0019	H-2(A) $\rightarrow$ LUMO(A) (50%) H-4(A) $\rightarrow$ LUMO(A) (26%) H-3(B) $\rightarrow$ L + 1(B) (14%)	H-5(A) $\rightarrow$ LUMO(A) (3%)
730	0.013	H-1(B) $\rightarrow$ LUMO(B) (21%) H-6(B) $\rightarrow$ LUMO(B) (16%) H-2(B) $\rightarrow$ LUMO(B) (15%) H-11(B) $\rightarrow$ LUMO(B) (13%)	H-14(B) $\rightarrow$ LUMO(B) (8%) H-3(B) $\rightarrow$ LUMO(B) (8%) H-4(B) $\rightarrow$ LUMO(B) (7%) H-9(B) $\rightarrow$ LUMO(B) (4%) H-5(B) $\rightarrow$ LUMO(B) (4%)
1021	0.006	H-6(B) $\rightarrow$ LUMO(B) (29%) H-11(B) $\rightarrow$ LUMO(B) (21%) H-2(B) $\rightarrow$ LUMO(B) (18%) H-1(B) $\rightarrow$ LUMO(B) (15%)	H-13(B) $\rightarrow$ LUMO(B) (5%) H-14(B) $\rightarrow$ LUMO(B) (4%) H-12(B) $\rightarrow$ LUMO(B) (4%) H-10(B) $\rightarrow$ LUMO(B) (2%)

<sup>a</sup>A = Alpha Molecular Orbital; B = Beta Molecular Orbital.

and a 0.5 wt % solution in water.<sup>24</sup> In both types of samples, a distinct, broad absorption band was observed, primarily centered at 720 nm, indicating significant absorption in the near-infrared (NIR) region. Moreover, the film sample exhibited an additional, intense band with an onset at around 500 nm, while the solution sample displayed an onset at around 500 nm, accompanied by a shoulder at 450 nm, along with local maxima at 383 and 353 nm. These observations provide robust support for the computed UV-visible optical spectrum of the complex under investigation, thereby validating the use of the theoretical calculation method.

**3.1.5. QTAIM Topological Analyses.** Using Bader's quantum theory of atoms in molecules (QTAIM), the characteristics of the intramolecular bonds present in  $(C_6H_{10}N_2)[CuCl_4]$  have been examined, along with the topological parameters within the selected BCPS.<sup>54–56</sup> The QTAIM-NCI graphs and the RDG isosurface are provided in Figure 6. The calculated values of  $\rho(r)$ ,  $\nabla^2\rho(r)$ ,  $G(r)$ ,  $V(r)$ ,  $\epsilon(r)$  parameters, and the  $E_{int}$  energies are compiled in Table 3.

It is concluded that our compound involves four intramolecular interactions for stabilization. According to the QTAIM graph, these interactions are formed between the Cl-anion and the H atoms of the  $[C_6H_{10}N_2]$  entity. These interactions are characterized by electron densities ranging from 0.040 a.u. (BCP3) to 0.0479 a.u. (BCP5), and their Laplacian of electron density varies from 0.0111 a.u. (BCP3) to 0.0877 a.u. (BCP1). The positive values of  $\rho(r)$  and  $\nabla^2\rho(r)$  indicate that  $CuCl_4$  is stabilized via strong H-bonding interactions (polar covalent) with  $(C_6H_{10}N_2)$ . The NCI index confirms this finding by the appearance of a blue spot between  $Cl_{21}/Cl_{23}$  and  $H-(C_6H_{10}N_2)$ , indicating the formation of H-bonding interactions for stabilization. These H $\cdots$ bondings are characterized by  $G(r)/\rho(r) < 1$ . Additionally, in BCP1 and BCP4, it is found that the ellipticity of electron density  $\epsilon(r)$  has low values equal to 0.005 au and 0.01 a.u. These results indicate that these two Cl $\cdots$ H interactions are stable and responsible for complex stability. The RDG analysis exhibits a sharp peak located in the range  $-0.03$  a.u., indicating the formation of H-bonding interactions between the two systems. It is noted that the high interaction energy ( $E_{int}$ ) is  $-52.51$  kJ mol $^{-1}$  (BCP1, BCP2, and BCP5). Behind the strong H-bonding interactions that appear between the two systems, the formation of two vdW interactions is noted between  $Cl_{23}\cdots H_6$  and  $Cl_{22}\cdots H_3$ . These interactions are well confirmed by the appearance of a green spot between these atoms in NCI index. Finally, it is concluded that the stability of the complex results from both hydrogen and van der Waals interactions that occur between  $CuCl_4$  and  $(C_6H_{10}N_2)$ .

**3.1.6. 3D-ELF/2D-LOL Theory.** An analysis of the chemical bonding nature within the active site involving  $CuCl_4$  and  $(C_6H_{10}N_2)$  was conducted using the localized orbital locator (LOL).<sup>57,58</sup> The LOL theory was explored to analyze the

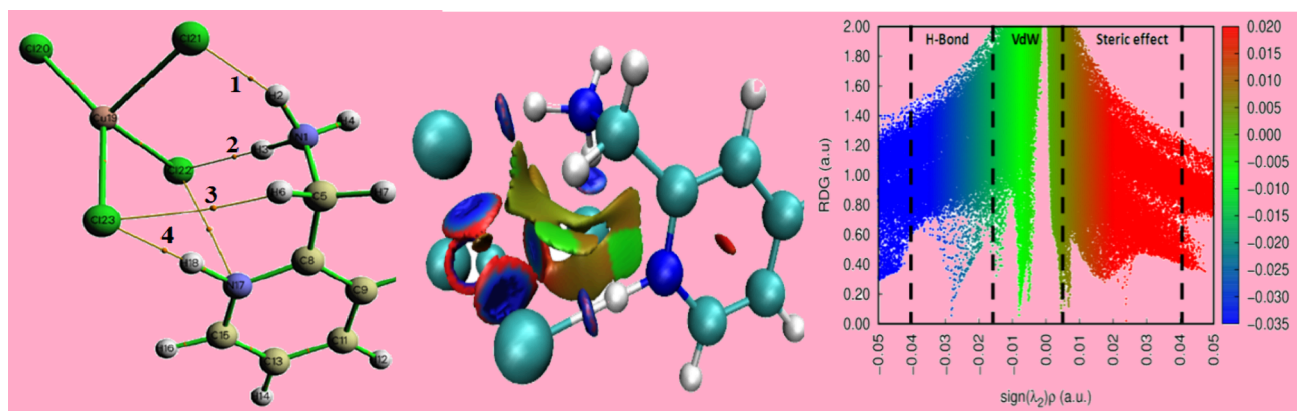


Figure 6. QTAIM graphs and NCI-RDG iso-surface ( $S = 0.5$  a.u.).

Table 3. Electron Density  $\rho(r)$ , Laplacian of Electron Density  $\nabla^2\rho(r)$ , Lagrangian Kinetic Energy Density  $G(r)$ , Potential Energy Density  $V(r)$ , Ellipticity of Electron Density  $\epsilon(r)$  in a.u., and Interaction Energy  $E_{\text{int}}$  in  $\text{kJ mol}^{-1}$  at the Selected BCPs in the Binding Regions of the  $(\text{C}_6\text{H}_{10}\text{N}_2)[\text{CuCl}_4]$  Complex

BCPs	$\rho(r)$	$\nabla^2\rho(r)$	$G(r)$	$G(r)/\rho(r)$	$V(r)$	$\epsilon(r)$	$E_{\text{int}}$
1	0.0455	0.0877	0.0292	0.64	-0.04	0.005	-52.51
2	0.0459	0.8426	0.0291	0.63	-0.04	0.003	-52.51
3	0.0040	0.0111	0.0023	0.47	-0.002	-1.29	-2.62
4	0.0097	0.308	0.0065	0.67	-0.005	0.14	-6.56
5	0.0479	0.0822	0.0301	0.62	-0.04	0.01	-52.51

topology of the most bonding  $\text{Cl}_{23}\cdots\text{H}_{18}$ . Additionally, electron localized function (ELF) analysis has been discussed to further elucidate the electronic distributions within the active area.<sup>59</sup> The red and blue colors obtained in the 2D-LOL and 3D-ELF maps confirmed the high delocalization of electrons and the localized electrons in the active regions.

From Figure 7a, it is evident that there is a red spot surrounding  $\text{H}_{18}$  located in front of a blue spot surrounding the  $\text{Cl}^-$  atom. This observation indicates the presence of electrons delocalized on the surface of  $(\text{C}_6\text{H}_{10}\text{N}_2)$  and an accumulation of electrons localized around chlorine, facilitating the formation of charge transfer between the two systems and suggesting a donor–acceptor couple. The same phenomena are observed for  $\text{Cl}-\text{CuCl}_4$  and  $\text{H}-(\text{C}_6\text{H}_{10}\text{N}_2)$ . Meanwhile, the high LOL value (red-yellow portions) responsible for the highly delocalized  $\pi$ -orbital varies from 0.64 to 0.80 a.u. This finding indicates a flux of electrons, inferring the formation of strong H-bonds. This result is well supported by the QTAIM topological analysis.

It is plausible that the  $(\text{C}_6\text{H}_{10}\text{N}_2)$  group exhibits better electron transfer delocalization characteristics accompanied by high surface electron activity. In Figure 7b, appearance of a white color surrounding the  $\text{H}_{18}$  atom and a black color surrounding the  $\text{Cl}_{23}$  atom suggests the existence of delocalized electrons on the surface of  $(\text{C}_6\text{H}_{10}\text{N}_2)$  and electrons localized on the surface of  $\text{Cl}-\text{CuCl}_4$ . This confirms the presence of charge transfer between the two systems. The 3D ELF plots show a dark red spot on the surface of the molecule  $(\text{C}_6\text{H}_{10}\text{N}_2)$ , indicating the majority accumulation of electrons localized in the active site, while chlorine has a weak localized electron concentration (Figure 7c).

This result suggests that charge transfer is occurring between the two systems, leading to the formation of a strong electrostatic bond that stabilizes the complex. This idea is fully supported by LOL and QTAIM analyses. Finally, it is

concluded that our system  $(\text{C}_6\text{H}_{10}\text{N}_2)$  is beneficial for increasing the charge accumulation on the surface, hence contributing to the high activity and stability of the  $\text{Cl}-\text{CuCl}_4$ - $(\text{C}_6\text{H}_{10}\text{N}_2)$  complex.

**3.1.7. Design of Solar Cell Structure.** The schematic representation of our structure is depicted in Figure 8. In this simulation, the  $(\text{C}_6\text{H}_{10}\text{N}_2)[\text{CuCl}_4]$  material is taken as the absorber and doped indium tin oxide (ITO) is used as the front contact.

A transparent ITO layer is chosen for its good conductivity, high transmission, and strong adhesion to charge carriers, making it a better option. A p-PTAA-type layer is used as an electron transport layer (ETL) and n- $\text{C}_{60}$  is used as a hole transport layer (HTL). The numerical model of  $(\text{C}_6\text{H}_{10}\text{N}_2)-[\text{CuCl}_4]$  PSCs was performed on TiberCAD (1 sun standard conditions,  $100 \text{ mW/cm}^2$ , AM1.5G, and ambient conditions of 300 K). Integrated input parameters for ITO, PTAA,  $(\text{C}_6\text{H}_{10}\text{N}_2)[\text{CuCl}_4]$ , and  $\text{C}_{60}$  (layer thickness, bandgap, electron affinity, dielectric permittivity, electron/hole mobility, electron/hole thermal velocity, defect density, etc.) were extracted from the previously published works<sup>14</sup> and are listed in Table 4. Gold was used as the back metal contact for the devices.

**3.1.8. Electrical Characteristics of  $(\text{C}_6\text{H}_{10}\text{N}_2)[\text{CuCl}_4]$  Photovoltaic Device.** In this section, we will focus on the performance of the photovoltaic device based on the  $(\text{C}_6\text{H}_{10}\text{N}_2)[\text{CuCl}_4]$  perovskite using the TiberCAD software. When the absorption spectrum, calculated through the DFT framework, is combined to investigate the output electrical performance of the  $(\text{C}_6\text{H}_{10}\text{N}_2)[\text{CuCl}_4]$  perovskite, the current–voltage characteristic, and the energy band profile at open circuit voltage obtained under exposure to the AM1.5G spectrum ( $100 \text{ mW cm}^{-2}$ ) are studied, as reported in Figure 9a.



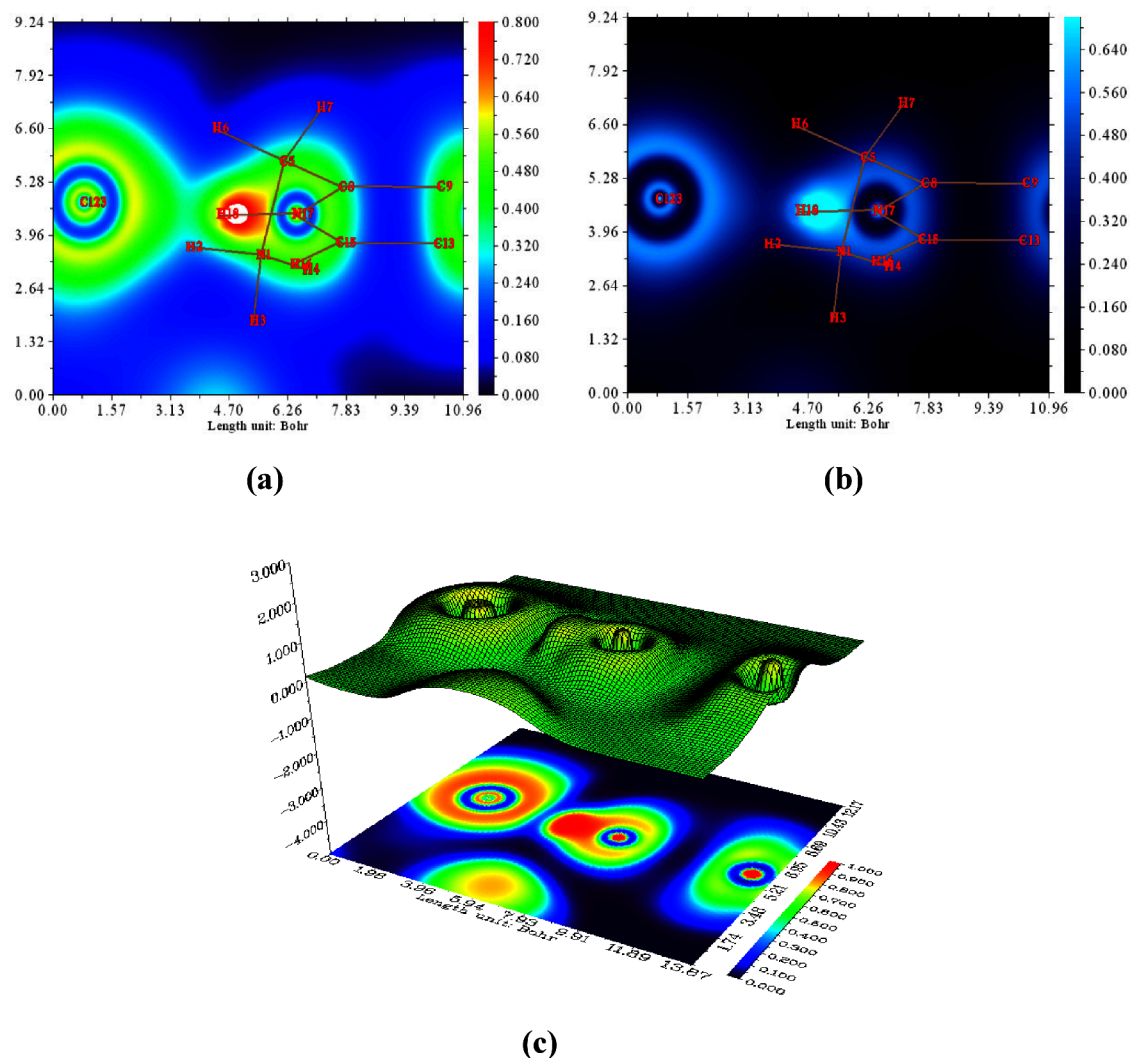


**Figure 7.** (a, b) 2D-LOL and (c) 3D-ELF, representing the electronic charge transfer between Cl-CuCl<sub>4</sub> and [C<sub>6</sub>H<sub>10</sub>N<sub>2</sub>].

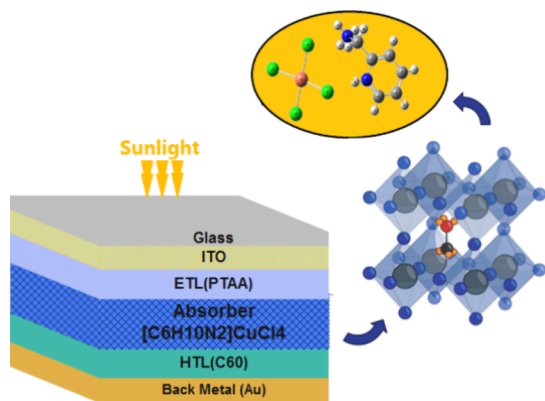


**Figure 8.** Design configuration of the (C<sub>6</sub>H<sub>10</sub>N<sub>2</sub>)[CuCl<sub>4</sub>] PSC.

The integrated current densities and the open circuit voltage extracted from the  $J$ - $V$  curves are illustrated in Figure 9b. The short-circuit current density and the open-circuit voltage are key parameters for achieving high conversion efficiency in the studied cell. Additionally, it is noted in Table 5 that the  $V_{oc}$  is better than 1.73 V, and the  $J_{sc}$  is 7.21 mA/cm<sup>2</sup>. The numerical modeling shows that the ITO/PTAA/(C<sub>6</sub>H<sub>10</sub>N<sub>2</sub>)[CuCl<sub>4</sub>]/C<sub>60</sub>/Au solar device has a FF of 81.34% and a PCE of 10.22%.

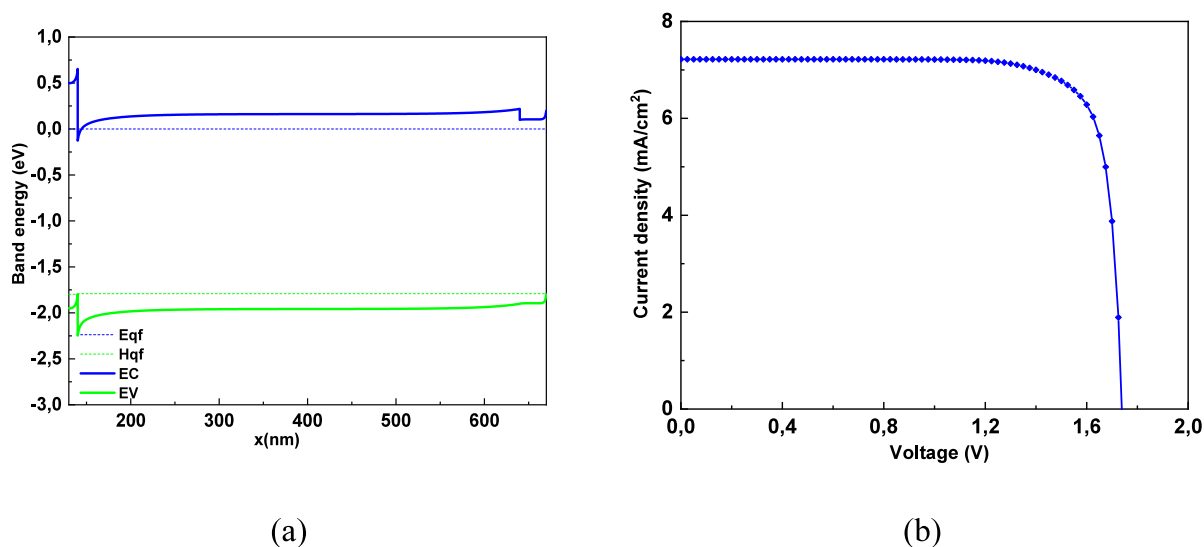
Our results are comparable to the study conducted by Zhu et al.,<sup>60</sup> as illustrated in the Table 5. The study focused on a solar cell utilizing MAPbBr<sub>3</sub> perovskite, known for its high band gap of approximately 2.3 eV, resulting in efficiencies slightly above 10.22%. Our absorbing material, (C<sub>6</sub>H<sub>10</sub>N<sub>2</sub>)[CuCl<sub>4</sub>], shows promise for applications in semitransparent solar cells and tandem-type cells. Furthermore, solar cell efficiency can be improved through various optimization parameters, such as the type and thickness of doped layers, the absorber layer, and doping level. Factors like temperature, humidity, and solar concentration also play a significant role in achieving optimal performance in solar cells.

#### 4. CONCLUSION

In this study, we extensively discuss the reorganization of inter- and intra-atomic contacts in the crystal packing through Hirshfeld surface analyses. It is revealed that the CuCl<sub>4</sub> entity forms robust bonding interactions with (C<sub>6</sub>H<sub>10</sub>N<sub>2</sub>). Electrical and electronic parameters (HOMO-LUMO,  $E_g$ , LHE, and PCE) demonstrated that the (C<sub>6</sub>H<sub>10</sub>N<sub>2</sub>)[CuCl<sub>4</sub>] complex is efficient for emerging generations of photovoltaic cells. The NCI theory, in conjunction with RDG isosurfaces, employs color codes to illustrate the stabilization of the examined complex through hydrogen bonding interactions. ELF/LOL

Table 4. Parameters Used for the Simulation of the Perovskite Solar Cell Structure Using TiberCAD

parameters	ITO	ETL(PTAA)	absorber ( $C_6H_{10}N_2$ )[CuCl <sub>4</sub> ]	HTL( $C_{60}$ )
thickness (nm)	130	10	500	30
band gap, $E_g$ (eV)	3.50	3.20	2.12	2.00
electron affinity (eV)	4.00	4.00	4.10	2.00
dielectric permittivity, relative $\epsilon_r$	11.7		13.60	5.00
effective conduction band density ( $1/cm^3$ )	$2.2 \times 10^{18}$	$1.00 \times 10^{20}$	$1.00 \times 10^{18}$	$2.2 \times 10^{19}$
effective valence band density ( $1/cm^3$ )	$1.8 \times 10^{19}$	$2.0010^{19}$	$1.00 \times 10^{18}$	$2.2 \times 10^{19}$
electron mobility, $\mu_n$ ( $cm^2 \cdot V^{-1} \cdot s^{-1}$ )	20	$1 \times 10^{-8}$	10	$1.00 \times 10^{-3}$
hole mobility, $\mu_p$ ( $cm^2 \cdot V^{-1} \cdot s^{-1}$ )	10	$1 \times 10^{-4}$	10	$1.00 \times 10^{-2}$
defect density, $N_t$ ( $1/cm^3$ )	$1.0 \times 10^{14}$	$1.0 \times 10^{14}$	$1.0 \times 10^{14}$	$1.0 \times 10^{14}$

Figure 9. Band energy (a) and the characteristics  $J-V$  (b) of the  $(C_6H_{10}N_2)[CuCl_4]$  solar cell.Table 5. Electrical Parameters of the  $[C_6H_{10}N_2]-CuCl_4$  Solar Cell

	$J_{sc}$ ( $mA/cm^2$ )	$V_{oc}$ (V)	FF (%)	PCE (%)
perovskite/MAPbBr <sub>3</sub> <sup>60</sup>	8.70	1.581	67.4	9.27
SCP <sup>a</sup> studied in this work	7.21	1.73	81.34	10.22

<sup>a</sup>SCP: solar cell parameters.

analyses distinctly confirm the presence of high electron concentrations in the binding sites. In our study on the  $(C_6H_{10}N_2)[CuCl_4]$  solar cell, we conducted a numerical simulation of cell performance using TiberCAD software. Fine-tuning the architecture of the perovskite structure involves adjusting the energy band profile and the electrical measurements. The maximum efficiency for this structure reached 10.22%. Consequently, this numerical model holds promise for predicting various hybrid perovskite solar cell-based 2D- and 3D-models under different climatic conditions, optimizing for maximum power efficiency.

## AUTHOR INFORMATION

### Corresponding Authors

**Sahbi Ayachi** – Laboratory of Physico-Chemistry of Materials (LR01ES19), Faculty of Sciences, University of Monastir, 5019 Monastir, Tunisia; Email: [ayachi\\_sahbi@yahoo.fr](mailto:ayachi_sahbi@yahoo.fr)

**Houcine Naili** – Laboratory Physico Chemistry of the Solid State, Department of Chemistry, Faculty of Sciences, University of Sfax, Sfax 3000, Tunisia; [orcid.org/0000-0002-9224-5851](https://orcid.org/0000-0002-9224-5851); Email: [houcine\\_naili@yahoo.com](mailto:houcine_naili@yahoo.com)

### Authors

**Bilel Chouchen** – Laboratory of Automatic, Electrical Systems and Environment (LAESE), The National Engineering School of Monastir (ENIM), University of Monastir, 5019 Monastir, Tunisia

**Noureddine Mhadhbi** – Laboratory Physico Chemistry of the Solid State, Department of Chemistry, Faculty of Sciences, University of Sfax, Sfax 3000, Tunisia; University of Monastir, Preparatory Institute for Engineering Studies of Monastir, 5019 Monastir, Tunisia

**Bouid Gassoumi** – Laboratory of Advanced Materials and Interfaces (LIMA), University of Monastir, Faculty of Sciences of Monastir, 5000 Monastir, Tunisia

**Intissar Hamdi** – Laboratory Physico Chemistry of the Solid State, Department of Chemistry, Faculty of Sciences, University of Sfax, Sfax 3000, Tunisia

**Hamid Hadi** – Department of Chemistry, Physical Chemistry Group, Lorestan University, Khorramabad 6815144316, Iran

**Matthias Auf der Maur** – Department of Electronic Engineering, University of Rome Tor Vergata, 00133 Rome, Italy

**Abdelkader Chouaih** – Laboratory of Technology and Solid Properties (LTPS), Abdelhamid Ibn Badis University of Mostaganem, Mostaganem 27000, Algeria

**Taoufik Ladhari** – Laboratory of Automatic, Electrical Systems and Environment (LAESE), The National Engineering School of Monastir (ENIM), University of Monastir, 5019 Monastir, Tunisia

Salvatore Magazù – Dipartimento di Scienze Matematiche e Informatiche, Scienze Fisiche e Scienze della Terra, Università di Messina, S. Agata 98166 Messina, Italy

Complete contact information is available at:  
<https://pubs.acs.org/10.1021/acsomega.4c00190>

### Author Contributions

B.C., B.G., N.M., H.H.: Conceptualization, Methodology, Software, Data curation, Writing—original draft, Supervision, Validation, Writing—review and editing. I.H., A.C., T.L.: Investigation, Validation, Conceptualization. S.M., M.A.d.M., H.N., S.A.: Software, Data curation, Visualization, Investigation, Review and editing.

### Notes

The authors declare no competing financial interest.

### ACKNOWLEDGMENTS

The authors extend their sincere appreciation to the Ministry of Higher Education and Scientific Research in Tunisia for the technical and financial support provided for this study, based on an agreement between the Ministry of Higher Education and Scientific Research in Tunisia and the American Chemical Society (ACS).

### REFERENCES

- (1) Raoui, Y.; Ez-Zahraouy, H.; Ahmad, S.; Kazim, S. Unravelling the theoretical window to fabricate high performance inorganic perovskite solar cells. *Sustainable Energy Fuels* **2021**, *5*, 219–229.
- (2) Bhattarai, S.; Das, T. D. Optimization of the perovskite solar cell design to achieve a highly improved efficiency. *Optical Materials* **2021**, *111*, 110661.
- (3) Travis, W.; Glover, E.N. K.; Bronstein, H.; Scanlon, D. O.; Palgrave, R. G. On the application of the tolerance factor to inorganic and hybrid halide perovskites: a revised system. *Chemical Science* **2016**, *7*, 4548–4556.
- (4) Merckx, T.; Aguirre, A.; Kuang, Y.; van der Heide, A.; Hajjiah, A.; Abdulraheem, Y.; Krishna, A.; Poortmans, J.; Aernouts, T. Stable Device Architecture With Industrially Scalable Processes for Realizing Efficient 784 cm<sup>2</sup> Monolithic Perovskite Solar Modules. *IEEE Journal of Photovoltaics* **2023**, *13*, 419–421.
- (5) Green, M. A.; Ho-Baillie, A.; Snaith, H. J. The emergence of perovskite solar cells. *Nat. Photonics* **2014**, *8*, 506–514.
- (6) Matteocci, F.; Rossi, D.; Castriotta, L. A.; Ory, D.; Mejaouri, S.; der Maur, M. A.; Sauvage, F.; Cacovich, S.; Di Carlo, A. Wide bandgap halide perovskite absorbers for semi-transparent photovoltaics: From theoretical design to modules. *Nano Energy* **2022**, *101*, 107560.
- (7) Kumar, N.; Rani, J.; Kurchania, R. Advancement in CsPbBr<sub>3</sub> inorganic perovskite solar cells: Fabrication, efficiency and stability. *Solar Energy* **2021**, *221*, 197–205.
- (8) Hajjiah, A.; Gamal, M.; Kandas, I.; Gorji, N. E.; Shehata, N. DFT and AMPS-1D simulation analysis of all-perovskite solar cells based on CsPbI<sub>3</sub>/FAPbI<sub>3</sub> bilayer structure. *Solar Energy Materials and Solar Cells* **2022**, *248*, 112026.
- (9) Grancini, G.; Roldán-Carmona, C.; Zimmermann, I.; Mosconi, E.; Lee, X.; Martineau, D.; Narbey, S.; Oswald, F.; De Angelis, F.; Graetzel, M.; Nazeeruddin, M. K. One-Year stable perovskite solar cells by 2D/3D interface engineering. *Nat. Commun.* **2017**, *8*, 15684.
- (10) Cho, E.; Kim, Y. Y.; Ham, D. S.; Lee, J. H.; Park, J.-S.; Seo, J.; Lee, S.-J. Highly efficient and stable flexible perovskite solar cells enabled by using plasma-polymerized-fluorocarbon antireflection layer. *Nano Energy* **2021**, *82*, 105737.
- (11) Kojima, A.; Teshima, K.; Shirai, Y.; Miyasaka, T. Organometal Halide Perovskites as Visible-Light Sensitizers for Photovoltaic Cells. *J. Am. Chem. Soc.* **2009**, *131*, 6050–6051.
- (12) NREL. Best Research-Cell Efficiency Chart Photovoltaic Research NREL, <https://www.nrel.gov/pv/cell-efficiency.html> (accessed September 2020).
- (13) Isikgor, F. H.; Zhumagali, S.; Merino, L. V. T.; De Bastiani, M.; McCulloch, I.; De Wolf, S. Molecular engineering of contact interfaces for high-performance perovskite solar cells. *Nat. Rev. Mater.* **2023**, *8*, 89–108.
- (14) Lin, L.; Jiang, L.; Li, P.; Xiong, H.; Kang, Z.; Fan, B.; Qiu, Y. Simulated development and optimized performance of CsPbI<sub>3</sub> based all-inorganic perovskite solar cells. *Solar Energy* **2020**, *198*, 454–460.
- (15) Lin, L.; Jones, T. W.; Yang, T.C.-J.; Duffy, N. W.; Li, J.; Zhao, L.; Chi, B.; Wang, X.; Wilson, G. J. Inorganic Electron Transport Materials in Perovskite Solar Cells. *Advanced Functional Materials* **2021**, *31*, 2008300.
- (16) Agresti, A.; Pazniak, A.; Pescetelli, S.; Di Vito, A.; Rossi, D.; Pecchia, A.; Auf der Maur, M.; Liedl, A.; Larciprete, R.; Kuznetsov, D. V.; Saranin, D.; Di Carlo, A. Titanium-carbide MXenes for work function and interface engineering in perovskite solar cells, *Nat. Mater.* **2019**, *18*, 1228–1234.
- (17) Hossain, M. K.; Arnab, A. A.; Das, R. C.; Hossain, K. M.; Rubel, M. H. K.; Rahman, M. F.; Bencherif, H.; Emetere, M. E.; Mohammed, M. K. A.; Pandey, R. Combined DFT, SCAPS-1D, and wxAMPS frameworks for design optimization of efficient Cs<sub>2</sub>BiAgI<sub>6</sub>-based perovskite solar cells with different charge transport layers. *RSC Advances* **2022**, *12*, 34850–34873.
- (18) Salih, M. A.; Mustafa, M. A.; Yousef, B. A. A. Developing Lead-Free Perovskite-Based Solar Cells with Planar Structure in Confined Mode Arrangement Using SCAPS-1D. *Sustainability* **2023**, *15*, 1607.
- (19) Huang, L.; Hu, Z.; Xu, J.; Sun, X.; Du, Y.; Ni, J.; Cai, H.; Li, J.; Zhang, J. Efficient electron-transport layer-free planar perovskite solar cells via recycling the FTO/glass substrates from degraded devices. *Solar Energy Materials and Solar Cells* **2016**, *152*, 118–124.
- (20) Yin, G.; Zhao, H.; Jiang, H.; Yuan, S.; Niu, T.; Zhao, K.; Liu, Z.; Liu, S. Precursor Engineering for All-Inorganic CsPbI<sub>2</sub>Br Perovskite Solar Cells with 14.78% Efficiency. *Advanced Functional Materials* **2018**, *28*, 1803269.
- (21) Montecucco, R.; Quadri, E.; Po, R.; Grancini, G. All-Inorganic Cesium-Based Hybrid Perovskites for Efficient and Stable Solar Cells and Modules. *Advanced Energy Materials* **2021**, *11*, 2100672.
- (22) Kim, J. Y.; Lee, J.-W.; Jung, H. S.; Shin, H.; Park, N.-G. High-Efficiency Perovskite Solar Cells. *Chem. Rev.* **2020**, *120*, 7867–7918.
- (23) Auf der Maur, M.; Matteocci, F.; Di Carlo, A.; Testa, M. Reverse bias breakdown and photocurrent gain in CH<sub>3</sub>NHPbBr<sub>3</sub> films. *Applied Physics Letters* **2022**, *120* (11), 113505.
- (24) Hamdi, I.; Khan, Y.; Aouaini, F.; Seo, J. H.; Koo, H. J.; Turnbull, M. M.; Walker, B.; Naili, H. A copper-based 2D hybrid perovskite solar absorber as a potential eco-friendly alternative to lead halide perovskites. *J. Mater. Chem. C* **2022**, *10*, 3738.
- (25) G09/Gaussian.com. <http://gaussian.com/glossary/g09/>.
- (26) Dennington, R.; Keith, T.; Millam, J. *GaussView*, version 5.0.8; Semiche Inc.: Shawnee Mission, KS, 2009.
- (27) Grimme, S. Semiempirical hybrid density functional with perturbative second-order correlation. *J. Chem. Phys.* **2006**, *124*, 034108.
- (28) Grimme, S.; Antony, J.; Ehrlich, S.; Krieg, H. A consistent and accurate ab initio parametrization of density functional dispersion correction (DFT-D) for the 94 elements H-Pu. *J. Chem. Phys.* **2010**, *132*, 154104.
- (29) Lee, C.; Yang, W.; Parr, R. G. Development of the Colle-Salvetti correlation-energy formula into a functional of the electron density. *Phys. Rev. B* **1988**, *37*, 785–789.
- (30) Hay, P. J.; Wadt, W. R. Ab initio effective core potentials for molecular calculations. Potentials for the transition metal atoms Sc to Hg. *J. Chem. Phys.* **1985**, *82*, 270–283.
- (31) Gao, Y.; Lu, Z.-B. Theoretical insight into the influence of different molecular design strategies on photovoltaic properties for a series of POM-based dyes applied in dye-sensitized solar cells. *New J. Chem.* **2023**, *47*, 9501–9507.



- (32) Wolff, S. K.; Grimwood, D. J.; McKinnon, J. J.; Jayatilaka, D.; Spackman, M. A. *Crystal Explorer 2.1*; University of Western Australia, Perth, 2007.
- (33) GaussSum Version 3.0. <https://gausssum.sourceforge.net/DocBook/index.html> (accessed June 3, 2023).
- (34) Lu, T.; Chen, F. Multiwfn: A multifunctional wavefunction analyzer. *J. Comput. Chem.* **2012**, *33*, 580–592.
- (35) Azeem, U.; Khera, R. A.; Naveed, A.; Imran, M.; Assiri, M. A.; Khalid, M.; Iqbal, J. Tuning of a A-A-D-A-A-Type Small Molecule with Benzodithiophene as a Central Core with Efficient Photovoltaic Properties for Organic Solar Cells. *ACS Omega* **2021**, *6*, 28923–28935.
- (36) Khalid, M.; Khan, M. U.; Shafiq, I.; Hussain, R.; Ali, A.; Imran, M.; Braga, A. A. C.; Fayyaz ur Rehman, M.; Akram, M. S. Structural modulation of  $\pi$ -conjugated linkers in D- $\pi$ -A dyes based on triphenylamine dicyanovinylene framework to explore the NLO properties. *Royal Society Open Science* **2021**, *8*, 210570.
- (37) Auf der Maur, M.; Povolotskyi, M.; Sacconi, F.; et al. TiberCAD: towards multiscale simulation of optoelectronic devices. *Opt Quant Electron* **2008**, *40*, 1077–1083.
- (38) Valeti, N. J.; Prakash, K.; Singha, M. K. Numerical simulation and optimization of lead free CH<sub>3</sub>NH<sub>3</sub>SnI<sub>3</sub> perovskite solar cell with CuSbS<sub>2</sub> as HTL using SCAPS 1D. *Results in Optics* **2023**, *12*, 100440.
- (39) Amjad, A.; Qamar, S.; Zhao, C.; Fatima, K.; Sultan, M.; Akhter, Z. Numerical simulation of lead-free vacancy ordered Cs<sub>2</sub>PtI<sub>6</sub> based perovskite solar cell using SCAPS-1D. *RSC Adv.* **2023**, *13*, 23211–23222.
- (40) Ashfaq, M.; Ali, A.; Tahir, M. N.; Kuznetsov, A.; Munawar, K. S.; Muhammad, S. Synthesis, single-crystal exploration, hirshfeld surface analysis, and DFT investigation of the thiosemicarbazones. *J. Mol. Struct.* **2022**, *1262*, 133088.
- (41) Arjun, H. A.; Anil Kumar, G. N.; Elancheran, R.; Kabilan, S. Crystal structure, DFT and Hirshfeld surface analysis of (E)-N'-[(1-chloro-3,4-di-hydro-naph-thal-en-2-yl)methyl-idene]benzohydrazide monohydrate. *Acta Cryst. E* **2020**, *76*, 132–136.
- (42) Ashfaq, M.; Bogdanov, G.; Ali, A.; Tahir, M. N.; Abdullah, S. Pyrimethamine-Based Novel Co-Crystal Salt: Synthesis, Single-Crystal Investigation, Hirshfeld surface analysis and DFT inspection of the 2,4-diamino-5-(4-chlorophenyl)-6-ethylpyrimidin-1-ium 2,4-dichlorobenzoate (1:1) (DECB). *J. Mol. Struct.* **2021**, *1235*, 130215.
- (43) Chérif, I.; Raissi, H.; Abiedh, K.; Gassoumi, B.; Caccamo, M. T.; Magazu, S.; Said, A. H.; Hassen, F.; Boubaker, T.; Ayachi, S. Exploration of intramolecular charge transfer in para-substituted nitrobenzofurazan: Experimental and theoretical analyses. *Spectrochimica Acta Part A: Molecular and Biomolecular Spectroscopy* **2023**, *301*, 122939.
- (44) Abad, N.; Sallam, H. H.; Al-Ostoot, F. H.; Khamees, H. A.; Al-horaibi, S. A.; A, S. M.; Khanum, S. A.; Madegowda, M.; Hafi, M. E.; Mague, J. T.; Essassi, E. M.; Ramli, Y. Synthesis, crystal structure, DFT calculations Hirshfeld surface analysis, energy frameworks, molecular dynamics and docking studies of novel isoxazolequinoxaline derivative (IZQ) as anti-cancer drug. *J. Mol. Struct.* **2021**, *1232*, 130004.
- (45) Alam, K.; Khan, I. M. Crystallographic, dynamic and Hirshfeld surface studies of charge transfer complex of imidazole as a donor with 3,5-dinitrobenzoic acid as an acceptor: Determination of various physical parameters. *Organic Electronics.* **2018**, *63*, 7–22.
- (46) Chérif, I.; Raissi, H.; Abiedh, K.; Gassoumi, B.; Teresa Caccamo, M.; Magazu, S.; Haj Said, A.; Hassen, F.; Boubaker, T.; Ayachi, S. Photophysical and nonlinear optical properties of para-substituted nitrobenzofurazan: A comprehensive DFT investigation. *J. Photochem. Photobiol., A* **2023**, *443*, 114850.
- (47) Gassoumi, B.; Mehri, A.; Hammami, H.; Castro, M.E.; Karayel, A.; Ozkinali, S.; Melendez, F.J.; Nouar, L.; Madi, F.; Ghalla, H.; Chaabane, R. B.; Ben Ouada, H. Spectroscopic characterization, host-guest charge transfer, Hirshfeld surfaces, AIM-RDG and ELF study of adsorption and chemical sensing of heavy metals with new derivative of Calix [4]quinone: A DFT-D3 computation. *Mater. Chem. Phys.* **2022**, *278*, 125555.
- (48) Mackenzie, C. F.; Spackman, P. R.; Jayatilaka, D.; Spackman, M. A. CrystalExplorer model energies and energy frameworks: extension to metal coordination compounds, organic salts, solvates and open-shell systems. *IUCrJ.* **2017**, *4*, 575–587.
- (49) McKinnon, J. J.; Jayatilaka, D.; Spackman, M. A. Towards quantitative analysis of intermolecular interactions with Hirshfeld surfaces. *Chem. Commun.* **2007**, 3814–3816.
- (50) Aihara, J. Reduced HOMO–LUMO Gap as an Index of Kinetic Stability for Polycyclic Aromatic Hydrocarbons. *J.Phys. Chem. A* **1999**, *103*, 7487–7495.
- (51) Mahmood, A.; Irfan, A.; Wang, J.-L. Machine Learning for Organic Photovoltaic Polymers: A Minireview. *Chin J. Polym. Sci.* **2022**, *40*, 870–876.
- (52) Mahmood, A.; Hu, J.; Tang, A.; Chen, F.; Wang, X.; Zhou, E. A novel thiazole based acceptor for fullerene-free organic solar cells. *Dyes Pigm.* **2018**, *149*, 470–474.
- (53) Eno, E. A.; Louis, H.; Unimuke, T. O.; Gber, T. E.; Mbonu, I. J.; Ndubisi, C. J.; Adalikwu, S. A. Reactivity, stability, and thermodynamics of para-methylpyridinium-based ionic liquids: Insight from DFT, NCI and QTAIM. *Journal of Ionic Liquids* **2022**, *2* (1), 100030.
- (54) Kumar, P. S. V.; Raghavendra, V.; Subramanian, V. Bader's Theory of Atoms in Molecules (AIM) and its Applications to Chemical Bonding. *J. Chem. Sci.* **2016**, *128*, 1527–1536.
- (55) Gassoumi, B.; Chaabane, M.; Ghalla, H.; Chaabane, R. B. Role of hydrogen bonding interactions within of the conformational preferences of calix[n = 4,6,8]arene: DFT and QTAIM analysis. *J. Mol. Model.* **2020**, *26*, 12.
- (56) Abdelaziz, B.; Chérif, I.; Gassoumi, B.; Patané, S.; Ayachi, S. Linear, and Nonlinear Optical Responses of Nitrobenzofurazan-Sulfide Derivatives: DFT-QTAIM Investigation on Twisted Intramolecular Charge Transfer. *J.Phys. Chem. A* **2023**, *127*, 9895–9910.
- (57) Yang, C.; Song, P.; Ma, F.; Li, Y. Enhanced Photovoltaic Property and Panchromatic Photocatalytic by Forming D- $\pi$ -A-bacteriochlorin Dyads: A Computational Investigation. *Solar RRL* **2023**, *7* (14), na.
- (58) Kumar, B. A.; Vetrivelan, V.; Ramalingam, G.; Manikandan, A.; Viswanathan, S.; Boomi, P.; Ravi, G. Computational studies and experimental fabrication of DSSC device assembly on 2D-layered TiO<sub>2</sub> and MoS<sub>2</sub>@TiO<sub>2</sub> nanomaterials. *Physica B: Condensed Matter.* **2022**, *633*, 413770.
- (59) Chérif, I.; Raissi, H.; Abiedh, K.; Gassoumi, B.; Caccamo, M. T.; Magazu, S.; Said, A. H.; Hassen, F.; Boubaker, T.; Ayachi, S. Computational studies on optoelectronic and nonlinear optical properties of para-substituted nitrobenzofurazan compound. *Materials Today Communications* **2023**, *35*, 106133.
- (60) Zhu, H.; Pan, L.; Eickemeyer, F. T.; Hope, M. A.; Ouellette, O.; Alanazi, A. Q. M.; Gao, J.; Baumeler, T. P.; Li, X.; Wang, S.; Zakeeruddin, S. M.; Liu, Y.; Emsley, L.; Grätzel, M. Efficient and Stable Large Bandgap MAPbBr<sub>3</sub> Perovskite Solar Cell Attaining an Open Circuit Voltage of 1.65 V. *ACS Energy Lett.* **2022**, *7*, 1112–1119.